Electrodeposited Cu thin layers as low cost and effective underlayers for Cu_2O photocathodes in photoelectrochemical water electrolysis

Alberto Visibile[a], Martina Fracchia[b], Tomasz Baran[c], Alberto Vertova[a,e], Paolo Ghigna[b,e], Elisabet Ahlberg[d], Sandra Rondinini[a,e], Alessandro Minguzzi[a,e*]

[a] Dipartimento di Chimica, Università degli Studi di Milano, Via Golgi 19, 20133 Milan, Italy

[b] Dipartimento di Chimica, Università degli Studi di Pavia, Viale Taramelli 13, Pavia, 27100, Italy

[c] SajTom Ligh Future LTD, Wezerow 37/1, 32-090 Slomniki, Poland

[d] Department of Chemistry and Molecular Biology, Gothenburg University, Kemivägen 4, 412 96 Göteborg, Sweden

[e] INSTM, Consorzio Interuniversitario per la Scienza e Tecnologia Dei Materiali, Via Giusti 9, Firenze, 50121, Italy

Corresponding author: Alessandro Minguzzi. Mail: alessandro.minguzzi@unimi.it Phone: +390250314224

Keywords: Water Splitting, Hydrogen evolution reaction, X-ray absorption spectroscopy, copper

Abstract

Cu_2O is one of the most studied semiconductors for photocathodes in photoelectrochemical water splitting (PEC-WS). Its low stability is counterbalanced by good activity, provided that a suitable underlayer/support is used. While Cu_2O is mostly studied on Au underlayers, this paper proposes Cu(0) as a low-cost, easy to prepare and highly efficient alternative. Cu and Cu_2O can be electrodeposited from the same bath, thus allowing in principle to tune the final material's physico-chemical properties with high precision with a scalable method.

Electrodes and photoelectrodes are studied by means of electrochemical methods (cyclic voltammetry, Pb underpotential deposition) and by ex-situ X-ray absorption spectroscopy (XAS). While the potential applied for the deposition of Cu has no influence on the bulk structure and on the

photocurrent displayed by the semiconductor, it plays a role on the dark currents, making this strategy promising for improving the material's stability. Au/Cu_2O and Cu/Cu_2O show similar performances, the latter having clear advantages in view of future use in practical applications.

The influence of Cu underlayer thickness was also evaluated in terms of obtained photocurrent.

1. Introduction

Finding suitable alternatives to fossil fuels relies on the use of renewable energy sources. These are intermittent and often localized, thus requiring the use of a proper energy vector, such as H_2. Photoelectrochemical water splitting is one of the most promising routes for renewable hydrogen generation, being a one-step process for sunlight-to-H_2 transformation in mild conditions[1–4].

In PEC-WS, the oxygen evolution reaction (OER) takes place at a photoanode:

$$H_2O \rightarrow \frac{1}{2}O_2 + 2H^+ + 2e^- \quad [1]$$

While the hydrogen evolution reaction (HER) takes place at a photocathode:

$$2H_2O + 2e^- \rightarrow 2H_2 + 2OH^- \quad [2]$$

An efficient semiconductor should present the following features:

- efficient sunlight absorption for high yield generation of excited states inside the semiconductor,
- suitable band gap energy to enable sunlight absorption,
- efficient charge separation to avoid recombination and ensuring a high quantum efficiency,
- proper bands position with respect to the equilibrium potentials of the desired half-reactions,
- high stability and photostability.

Semiconductors able to perform reactions 1) and 2) without undergoing photodegradation typically have a wide band gap that limits the absorbed portion of the solar spectrum (e.g. TiO_2 with a 3 eV band gap can absorb only in the UV range) [5].

In the research of suitable photocathodes, Cu_2O is one of the most studied ones since:

- it presents a 2.17 eV band gap[6]. This value is high enough to have the proper energy to drive water electrolysis by visible light absorption.
- it presents suitable bands position, allowing both the hydrogen evolution reaction (HER) and the OER[7].
- it is made of abundant and low-cost elements.
- is non-toxic. This is an advantage if compared to other semiconductors for PEC-WS containing As, Cd and other toxic metals.
- it can be easily and reproducibly synthetized by several methods, including electrodeposition.

The bands position in Cu_2O satisfy the above mentioned requirements having a conduction band (CB) edge potential of -1.4 V, far above the energy corresponding to the H^+/H_2 couple (-0.65 V) and with the valence band (VB) edge energy at +0.77 V, that is slightly below the energy corresponding to the O_2/H_2O couple (+0.81 V) at pH = 7[8–10].

This semiconductor can be synthetized with a wide range of methods: thermal oxidation[11, 12], sol-gel[13] and solvothermal methods[14, 15], chemical vapour deposition[16], sonochemical synthesis[17], hydrothermal[18–20] and electroless[21] deposition. Sputtering is also used for the preparation of thin films with high homogeneity, low cost and easy synthesis[22]. State-of-the-art photocurrents were achieved by using electrodeposition from a $CuSO_4$ solution with lactic acid and the pH shifted to pH 12[23]. This electrodeposition bath for Cu_2O was firstly reported by Golden[24],

and lately used by several Authors [25–30] to easily obtain Cu_2O. The method guarantees high uniformity of the layer and the possibility of controlling the morphology and the size of the particles and the thickness of the layer together with their properties[31, 32] by simply varying the potential, the temperature, the pH or the deposition time.

A high pH is mandatory for preparing the p-type Cu_2O[33, 34], while the n-type semiconductor is obtained working at low pHs, [26, 35] but the reason is still under discussion[36]. The presence of lactic acid is needed to avoid the precipitation of copper hydroxide at pH 12.

Comparable photocurrent values are unusual in the current literature: Nian et al. [37] obtained only a maximum photocurrent of -0.025 $mA \cdot cm^{-2}$ on FTO, whereas most of the works report photocurrent higher than 1 $mA \cdot cm^{-2}$. This can be due to slight variations in the preparation procedure, concerning temperature, pH and presence of impurities. As we will show here, the support and the presence of an underlayer plays a crucial role as well.

Different underlayers can have an influence on grains size, shape and film orientation, in turn leading to different activities, as was shown in the case of Cu_2O films electrodeposited on ITO/glass, FTO/glass and ITO/PET [38]. On ITO/Glass there is the formation of Fernlike stellar dendrites with (111) orientation, on FTO/glass the dendrite like-crystal have (200)-preferred orientation while on ITO/PET more dense and truncated polyhedral grain with relatively (111) preferred crystal was found. EIS evidenced that the charge transfer resistance of FTO/Glass-Cu_2O exhibits lower values compared to the other substrates. Wang et al., working on silica substrates, noticed that changes in the pore diameter of the supporting silica leads to changes in Cu_2O nanoparticles dimension with subsequent modification of the semiconductor optical properties (band gap and absorption spectra)[39].

Thin films of Cr/Au have been used as underlayer[40] to increase the reproducibility of the recorded photocurrents and to improve the conductivity of the electrode and thus the probability of charge separation[41]. According to the literature, the use of only Au as underlayer can enhances light

absorption with localized surface plasmon resonance and scattering events[42], and by increasing the lifetime of the electron-hole couple[43]. From Lan et al.[44, 45] an increase in photocurrent is clearly observed in the presence of Au. However, it is not possible to evaluate the actual photocurrent values since the dark current values are not reported.

One of the main drawbacks of PEC-WS is the actual cost, preventing this technology to be competitive and sustainable. For example, using an expensive Au (or Cr/Au) underlayer deposited by poorly available techniques, may counterbalance the advantages of Cu_2O in terms of the final electrode's cost. Moreover, the European Union is going to ban chromium (VI) from all industrial processes and developing a technology using this material is quite unsatisfactory[46].

Some works reported the growth of Cu_2O on Cu, as such or obtained from Cu oxidation, but with conflicting results. Cu_2O deposited by comproportionation on a Cu mesh starting from Cu^{2+} by Jin et al. [47], obtained high performances, but the lack of transparency of the substrate requires further improvements. Tang et al. [48] with a similar synthesis obtained very different results in terms of photocurrent. Finally, Jung et al. [49] show that the presence of an unreacted Cu layer under Cu_2O inhibits the photoelectrical performance of Cu_2O-based photocathodes.

Aim of the present paper is to demonstrate that Cu is an effective alternative to the Cr/Au or Au underlayers, being low-cost, easy-to-prepare, sustainable and highly performant. Cu deposition does not require expensive techniques, since it is easily deposited by electrochemical methods obtaining flat and homogeneous surfaces. This can be done using the same deposition bath as for the semiconductor. Finally, Cu and Au have quite similar resistivity: 1.59 and 2.44×10^{-8} Ωm, respectively[50]. The advantage of electrochemical deposition arises in the possibility of finely tuning the layer properties as well as in obtaining a very thin layer, allowing the electrode to be partially transparent. This is an essential characteristic in a photoelectrochemical device. Moreover, with electrodeposition it is also possible to work with different types of conductive substrates.

Here we show that Cu(0) is not merely a reagent for the formation of an active Cu_2O photoelectrode, but is definitely a critical element in the electrode final performance. To show the role of the underlayer we compare the same Cu_2O layer on 3 different underlayers, namely FTO, Au and Cu(0).

All electrodes were characterized in term of morphology and chemical composition, by means of Electrochemical Impedance Spectroscopy, EIS, Under Potential Deposition, UPD, and ex-situ X-ray Absorption Spectroscopy.

The paper shows that the Cu underlayer holds the same advantages of the Au one; the influence of the physicochemical characteristics of the underlayer on the final photoelectrode performance is also discussed.

2. Materials and methods

2.1 Cu_2O and Cu(0) electrodeposition:

The photoelectrodes studied and compared are:

- Cu_2O@FTO as reference in the absence of underlayer.
- Cu_2O@Cu(-0.55 V)@FTO as proposed photocathode for PEC-WS.
- Cu_2O@Cu(-0.25 V)@FTO as proposed photocathode for PEC-WS.
- Cu_2O@Au@FTO as reference material in the literature.

Fluorine doped tin oxide (Aldrich) was cleaned in water and acetone in an ultrasound bath (10 min each) and dried at 80°C before use.

Cu_2O and Cu(0) are deposited from an aqueous solution of 0.2 M $CuSO_4$, 0.5 M K_2HPO_4 and 3 M lactic acid, to which 2 M aqueous KOH is slowly added until pH 12 is reached. The selected bath was previously studied by means of X-ray Absorption Spectroscopy to evaluate its stability[51].

The Cu(0) metallic underlayer was deposited at two different potentials, according to the deposition peaks found in the electrochemical analysis of the deposition bath (see the Results section). The deposition was carried out at 30°C and under stirring to guarantee a homogeneous deposit.

Au (about 200 nm) underlayers were prepared on a previously cleaned FTO using physical vapour deposition (PVD). For selected measurements (XRD, EIS and SEM) an Au disk electrode was used as substrate.

Cu_2O layers were electrodeposited in an unstirred bath at 0.55 V vs RHE in a 3-electrode cell configuration. According to the literature, the highest photocurrents are expected by deposition under galvanostatic conditions[29, 52] and at $T \approx 30$ °C[53]. However, we obtained better results under potentiostatic conditions and at 60 °C. In particular, the potential control allows controlling grain size, shape and composition[30, 54, 55], while the higher temperature allows for faster deposition and higher final performances[56]. At 60 °C, a sealed cell is required to avoid solution evaporation and changes in bath concentration during the deposition. A Saturated Calomel Electrode (SCE) was used as reference in a 0.5 M KNO_3 double bridge. The use of the double bridge avoids Cl^- contamination in the deposition bath, thus avoiding Cl^- doping of the material (leading to a possible n-type conductivity), and at the same time preserves the stability of the SCE in the alkaline environment. All the potentials are referred to the RHE electrode ($E_{RHE} = 0.059 \cdot pH + 0.244$ V). A 1x2 cm^2 Pt foil was used as counter electrode seated at almost 1 cm distance in front to the working electrode to ensure the formation of a homogeneous layer of Cu_2O, due to the good current distribution. The same electrodeposition procedure was used on all the different underlayers tested in this work. In the case of Cu_2O@FTO, an additional step is introduced before the potentiostatic deposition at 0.55 V vs RHE. In order to overcome the induction potential of Cu_2O deposition over FTO (**Fig 2**), a LSV from 0.75 to 0.25 V vs RHE at 10mVs^{-1} was performed to grow a thin layer of Cu_2O on the FTO surface.

One solution batch is stable enough to be used for the depostion of several electrodes (10 Cu_2O + 10 Cu),with good reproducibility.

The total amount of semiconductor and metallic Cu, to form a Cu_2O@Cu(0) electrode, was controlled by integrating the current during the deposition. In all deposits the total charge was set to 0.47 $C \cdot cm^{-2}$ for Cu(0) and to 0.5 $C \cdot cm^{-2}$ for Cu_2O.

All electrochemical depositions were performed with a CHI633d potentiostat/galvanostat inside a Faraday cage. All potential values are converted to the reversible hydrogen electrode (RHE) scale.

2.2 Physicochemical characterizations.

Electrochemical Impedance Spectroscopy (EIS):

Cu_2O was deposited onto an Au disk adopting the procedure described above. The considered potential window is between +0.56 and +0.16 V vs RHE in a de-aerated solution of NaH_2PO_4 0.5 M + NaOH 0.5 M (pH 11). In this window, no faradic reactions are evident. The frequency is varied between 100 kHz and 0.1 Hz, in the selected potential window. The amplitude was set to 10 mV. The capacitance was calculated for five different frequencies chosen for the analysis: 1 Hz, 10 Hz, 220 Hz, 1 kHz and 6 kHz. Those measurements were performed with a Princeton Applied Research (PAR) Parstat 4000+ using a Faraday cage to reduce any electrical noise.

Under Potential Depositions (UPD) were carried out in a 0.01 M $Pb(OAc)_2$ 0.5 M $NaClO_4$ + 0.001 M $HClO_4$ aqueous solution at pH 5.5[57, 58] previously purged with nitrogen.

The Cu electrode is immersed in the solution without $Pb(OAc)_2$ to obtain a background CV recorded from 0.422 to 0.122 V vs RHE to ensure that no faradic reactions occur in the absence of the Pb redox species. The background CV will be later subtracted from the UPD one.

After addition of $Pb(OAc)_2$ a CV (one cycle) is recorded in the same potential windows. It is important to test the electrode for UPD immediately after the deposition of the Cu layer. UPD peak areas are determined by integration using Origin 2016® and considering only the first half cycle.

Photocurrent measurement. All photoelectrodes were tested in an optical glass cell with a flat window in 0.5 M $NaHPO_4$ + 0.5 M NaOH (pH11) purged with nitrogen for 30 minutes. The counter electrode was a platinum foil while the reference was an SCE in a 0.5 M KNO_3 double bridge. On each electrode, a Linear Sweep Voltammetry (LSV) was carried out under pulsed light at the scan rate of $10mV \cdot s^{-1}$ from 0.523 V to 0.13 V vs RHE. The measurements were performed in a closed metal box able to prevent electrode ambient lighting and working as a Faraday cage as well.

The photocurrents were recorded using a Princeton Applied Research (PAR 263) potentiostat/galvanostat and a high intensity monochromatic LED (LEDENGINE LZ1-00G102) (λ=523 nm) was used for the study of the underlayer and of the semiconductor loading. In order to be able to compare the results with different underlayers, the LED distance was kept at 7 cm from the cell, while the sample distance from the cell border was as small as possible (~ 1 mm). Photocurrent comparisons with different underlayers were recorded with an Autolab PGSTAT204 potentiostat/galvanostat and a solar simulator (1.5 AM, LOT Oriel). Light was shuttered manually.

Electron Microscopy; Detailed analysis of the microstructure and chemical composition were performed using a Zeiss LEO ULTRA 55 FE-SEM scanning electron microscope (SEM) equipped with an Oxford Instrument INCA X-sight energy dispersive X-ray spectroscopy (EDX) system on a Cu_2O@Cu(0) sample with different magnification from 1000x to 100000x.

X-ray Diffraction (XRD); XRD was performed using a Siemens D5000 diffractometer with a grazing angle of 4 degrees to reduce the influence of the substrate and being able to evaluate the semiconductor only. The results were analyzed with DIFFRAC.SUITE EVA with PLU2019 – PDF-4+ 2019 RDB database.

Diffuse reflectance spectra (DRS); DRS spectra in UV-Vis range were recorded using a UV-3600 spectrophotometer (Shimadzu) equipped with an integrating sphere. $BaSO_4$ was used also as a reference material.

X-ray Absorption Spectroscopy (XAS). XAS measurements were performed in the fluorescence mode at the LISA beamline (BM08) at the European Synchrotron Radiation Facility (ESRF) at the Cu K-edge. A Si(311) double crystal monochromator was used; the harmonic rejection was realized by Pd mirrors with a cut-off energy of 20 keV, and a High Purity Germanium fluorescence detector array (13 elements) was used. The energy calibration was performed by measuring the absorption spectrum of metallic copper foil at the Cu K-edge (Cu K-edge: 8979 eV). The energy stability of the monochromator was checked by measuring the absorption spectrum of a Cu foil several times during the experiment. All data were obtained at room temperature. Spectra of standard samples CuO and Cu_2O, were acquired in the transmission mode. For those measurements a proper amount of sample (as to give a unit jump in the absorption coefficient) was mixed to cellulose and pressed to form a pellet.

The signal extraction was performed by means of the ATHENA code[59, 60]. For the X-ray Absorption Near Edge Structure (XANES) analysis, the raw spectra were first background subtracted using a straight line, and the normalized to unit absorption at 800 eV above the edge energy, where the EXAFS oscillations are not visible anymore. The EXAFS (Extended X-ray Absorption Fine Structure) data analysis was performed by using the EXCURVE code, using a k^2 weighing scheme and full multiple scattering calculations. The goodness of fit (GOF) is given by the F-factor:

$$F = 100 \sum_i^N \frac{[\chi_{\mathrm{i,exp}} - \chi_{\mathrm{i,calc}}]^2}{\sigma_i} \quad [3]$$

3. Results and Discussion

3.1 Voltammetric study

To address the potential window of interest for the electrodepositions, a series of linear sweep voltammetries (LSV) between 0.96 V and -0.84 V vs RHE were recorded considering all components of the deposition bath. The considered solutions are, therefore:

I. KOH 2M diluted until pH 12

II. K_2HPO_4 0.5 M + KOH 2M until pH12

III. K_2HPO4 0.5 M + lactic acid 3 M + KOH 2 M until pH 12

IV. K_2HPO_4 0.5 M + lactic acid 3 M + $CuSO_4$ 0.2 M + KOH 2 M until pH 12

This approach allowed also to test the potential stability window of each solution.

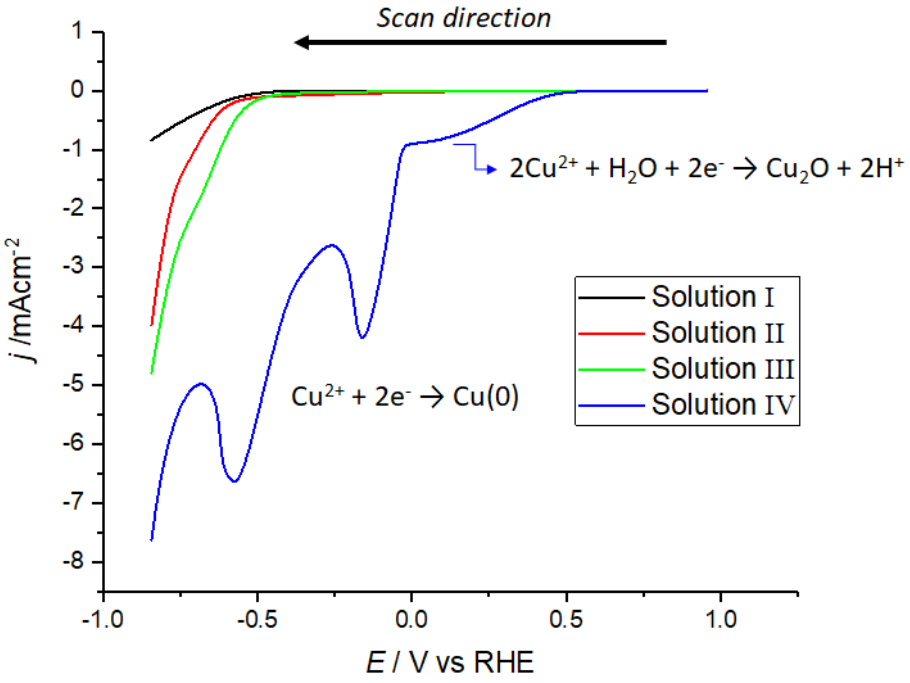

Fig 1 LSVs obtained using FTO as the working electrode in: black line: 2 M KOH pH 12; red line: 0.5 M K_2HPO_4 + 2 M KOH pH12; green line: 0.5 M K_2HPO_4 + 2 M KOH + 3 M lactic acid (LA) pH 12; blue line: 0.2 M $CuSO_4$ + 0.5 M K_2HPO_4 + 3 M lactic acid at pH 12 (addition of 2 M KOH). Scan rate 10 mVs^{-1}, Pt counter electrode

The LSVs reported in **Fig 1** clearly show that no peak is recorded in the absence of $CuSO_4$. Hydrogen evolution starts at about -0.5 V. The slight increase of current in the presence of lactic acid does not justify its reduction, while the small shoulder just before the HER in the presence of K_2HPO_4 (II) and then lactic acid (III) is probably due to oxygen reduction and cannot be related to the much more intense peak observed in the presence of Cu ions. In the presence of $CuSO_4$, a first shoulder is observed at ≈0.4 V vs RHE and two well-defined peaks are observed at -0.1 and -0.55 V vs RHE (blue line in **Fig 1**). The two large peaks are assigned to Cu deposition while, according to the literature, the shoulder is related to Cu_2O deposition[61] from a Cu^{2+} free solution (according to the complexation equilibrium with lactate). The presence of two peaks is likely due to the existance of two different nucleation sites and/or to two types of preferential orientation growth.

In alternative, the less cathodic peak could be related to the reduction of the already deposited Cu_2O[62] , but this possibility is not supported by the peak charge integration.

Subsequent cycles show that the potential of Cu(0) deposition peaks does not change, while deposition of Cu_2O occurs at more positive potentials (**Fig 2**). This behavior can be explained by considering that an induction potential is needed for the formation of the first grains of Cu_2O on the bare FTO surface while the same does not occur in the presence of a layer of Cu_2O, Cu(0) or Au. It is possible to notice the negative shift due to the higher energy required for grain formation.

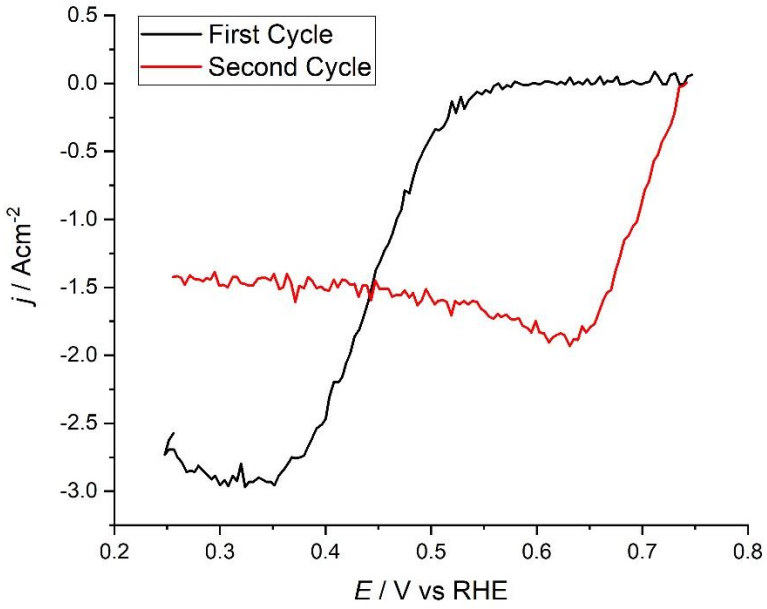

Fig 2 Linear Sweep Voltammetry (LSV) comparison between Cu_2O deposition peak on FTO free surface (in black) and on FTO surface in the presence of already deposited Cu_2O on it (red line). Scan rate 10 mVs^{-1}, Pt counter electrode

3.2 Characterization of the Cu_2O film

To prove the nature and the morphological feature of the Cu_2O deposit, scanning electron microscopy (SEM, Energy-dispersive X-ray spectroscopy (EDX) and X-ray Diffraction (XRD) were employed.

As evidenced by **Fig 3**, no significant differences in size or morphology were noticed on the Cu_2O deposited on Cu(0) and the one deposited on Au. Even if the particles are not geometrically defined, their size range between 50 and 200 nm. This is in agreement with Bijiani et al.[63], while other papers shows a higher order of magnitude (i.e.1000-2000 nm[25, 64]). This is an interesting result suggesting a larger real surface area for the present material and thus a larger surface available for charge transfer. Moreover, a reduced size of the particles increases their stability[65] and their photocatalytic efficiency by changing the light scattering properties[66]. On the other hand, smaller particles are likely associated with a higher number of surface defects and thus to a higher number of recombination centers. In addition, in the present work, it was possible to reach this results without

the use of any surfactants or organic solvent, sometimes adopted to control the crystallite size and morphology[67].

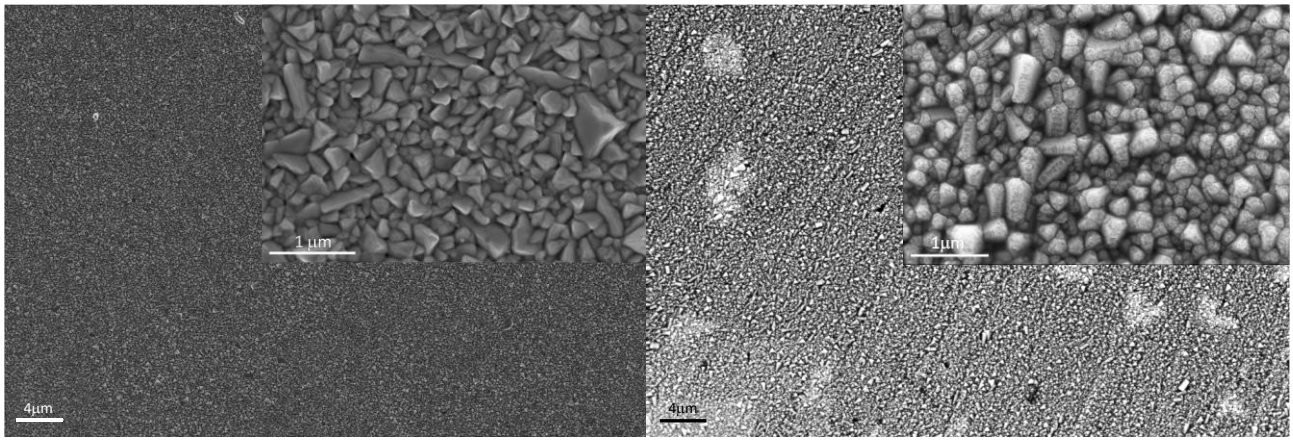

Fig 3 SEM images of a p-type Cu_2O@Cu(-0.25 V)@FTO (left) and Cu_2O@Au@FTO (right) samples . Different magnifications were used: main picture 5000x, inset 60000x

EDX analysis confirms the presence of Cu_2O: the Cu:O atomic ratio is equal to 63:37, which corresponds to the Cu_2O formula within the experimental error (*ca.* 5%). The lower Cu amount with respect to the 1:2 atomic ratio could be also explained by the presence of Cu vacancies, considered the main actor in the p-type conductivity of this material. As evident from **Fig 1** and from XRD results, **Fig 4**, the formation of metallic Cu at a deposition potential of 0.55 V can be excluded.

The X-ray diffraction patterns of Cu_2O@Cu(-0.55V)@FTO and Cu_2O@Au electrodes are shown in **Fig. 4.** A calculated pattern for the Cu_2O structure is also shown. In the pattern of the Cu_2O@Cu(-0.55V)@FTO electrode (green curve), the characteristic peaks of the Cu_2O phase, of metallic copper and of FTO can be identified. For what concerns the pattern of the Cu_2O@Au electrode (blue curve), the peaks of Cu_2O and Au can be observed. Comparing the peaks of Cu_2O in the patterns of the two electrodes with the simulated pattern (orange curve), it can be noted that the (111) facet reflection (2ϑ = 37°) [68][69] has an enhanced intensity with respect to all other peaks, indicating a preferential orientation of the Cu_2O grains along this crystallographic direction. This behavior was expected

working at pH 12[35, 70], and this is also the most active facet for photoelectrochemical purpose [40, 71]. The average size of the Cu_2O grains was evaluated for both samples with the Debye-Scherrer equation, resulting into 30 nm for Cu_2O@Au and 50 nm for Cu_2O@Cu(-0.55V)@FTO.

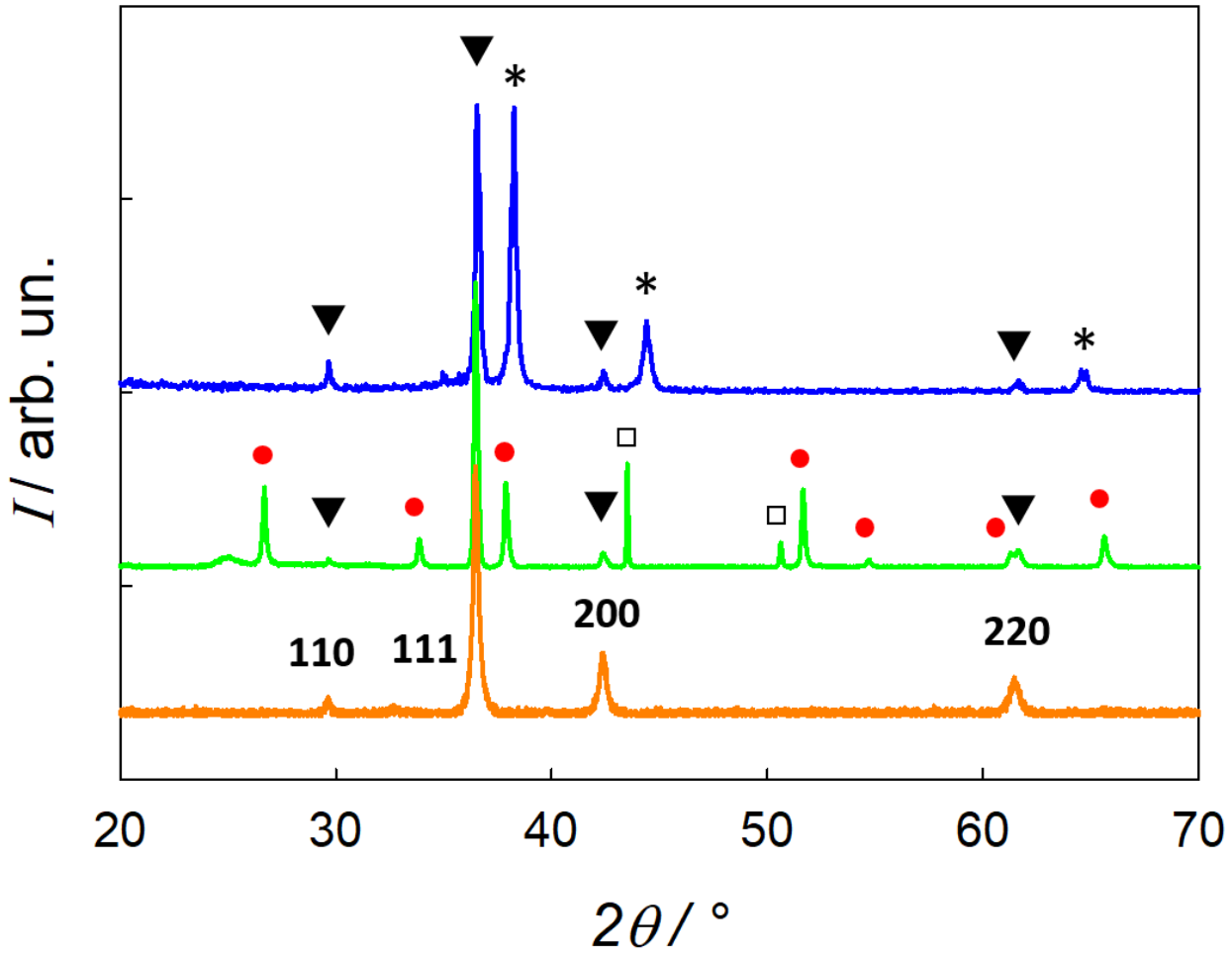

Fig 4 X-ray diffraction pattern for Cu_2O@Au (blue line), Cu_2O@Cu(-0.55 V)@FTO (green line) and calculated pattern for the Cu_2O structure (orange line). The black triangles indicate the peaks corresponding to the Cu_2O phase, the red circles identify the peaks corresponding to FTO, while the asterisks and the white squares are related to the peaks of metallic gold and copper, respectively. The Cu_2O@Au@FTO diffraction patter was obtained with grazing angle XRD (4 degrees)

EIS spectra were recorded to collect information on the p-type behavior of the Cu_2O@Au electrode through the evaluation of Mott-Schottky plots.

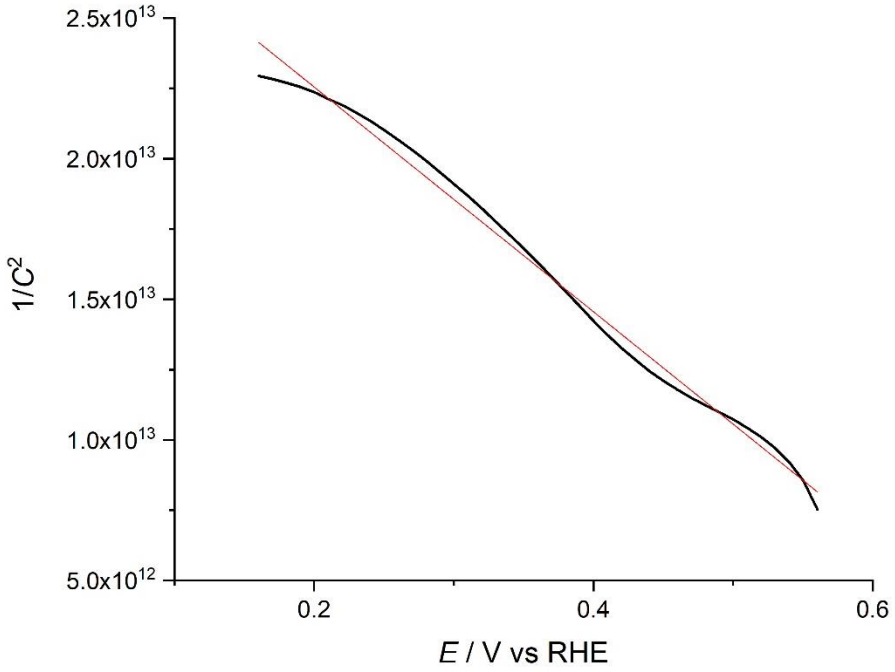

Fig 5 Mott-Schottky plot at 220 Hz of a Cu_2O@Au samples in Na_2SO_4 0.1M solution (black line). Counter electrode: Pt. The red line represent the linear fit described by equation [4]

The Mott-Schottky plot (**Fig 5**) indicates a negative slope, as expected from a p-type semiconductor. The linear data fit allows to obtain carrier concentration and flat band potential:

$$\frac{1}{C^2} = \frac{2}{e\varepsilon\varepsilon_0 N_A}\left(E - E_{fb} - \frac{kT}{e}\right) \qquad [4]$$

Where e is the elemental charge (1.602×10^{-19} C), ε_0 is the vacuum permittivity (8.85×10^{-12} F·m^{-1}), ε is the Cu_2O dielectric constant (6.6)[72], N_A is the hole carrier density and k is the Boltzmann constant (1.38×10^{-23} J·K^{-1}).

The calculated flat band potential (close to the valence band edge energy), is 0.79 V vs RHE.

The line slope allows the determination of the density of acceptor sites, (N_A) of 1.09×10^{18} cm^{-3}. These results are in good agreement with the values proposed in the literature for Cu_2O ($N_A = 5 \times 10^{17}$cm^{-3} and E_{fb} = 0.75 vs RHE)[25].

3.3 Effect of the deposition potential

After having confirmed the nature and the physicochemical features of the Cu_2O deposit, a deeper analysis of the electrodeposition phenomena is needed. One of the main interest of this work is to verify the possibility of depositing the Cu underlayer from the same deposition bath of the semiconductor. To this aim, we considered two potential values for the electrodeposition of Cu from the lactate solution. These correspond to the two cathodic peaks described in **Fig 1**. We can see that, at -0.55 V currents are more than 2 times higher than at -0.25 V because of the more negative applied potential with possible severe influences on the average grains size, shape and preferential grain orientation.

For what concerns the currents (recorded at 0.55 V vs RHE) of Cu_2O deposition on different supports (**Fig 6**), these are comparable but for the case of the Au support (blue line) that leads to slightly higher values, likely due to the slightly lower average crystallite size (XRD). The potentiostatic current-time measurements show the same shape, confirming for Cu_2O grown on Cu and Au underlayer a similar nucleation and growth mechanism if the same potential is applied.

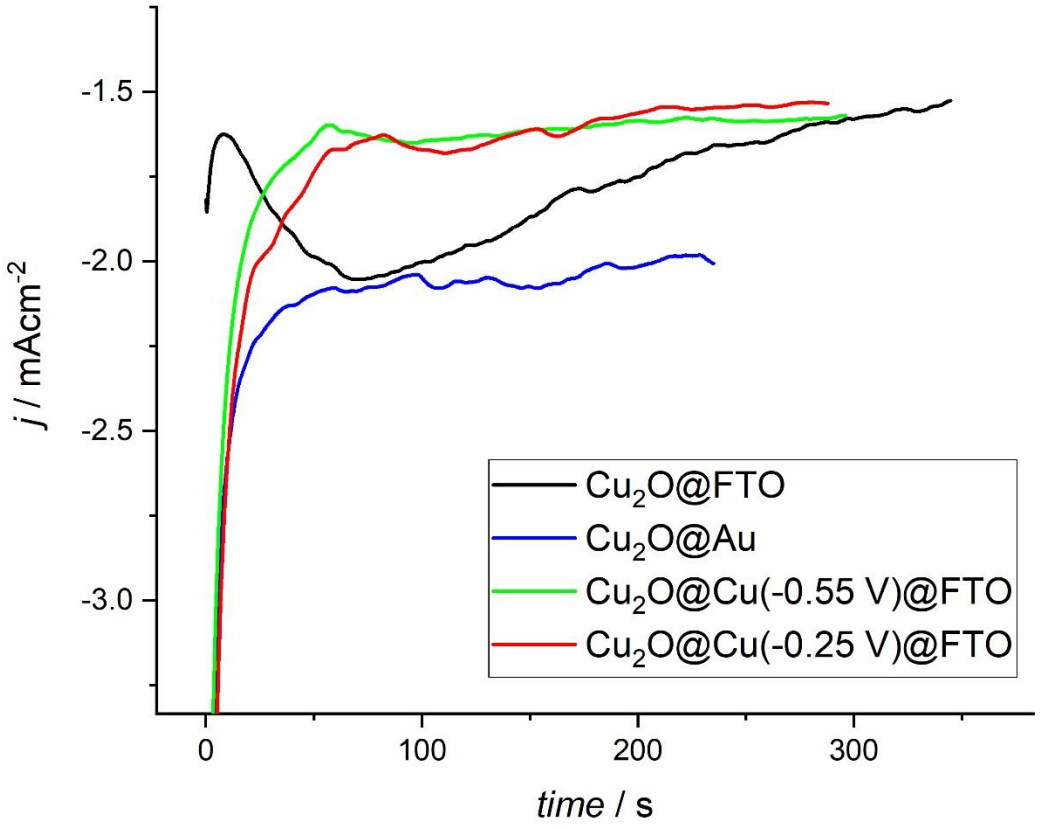

Fig 6 Deposition currents recorded at 0.55 V vs RHE during Cu_2O deposition on different substrates; FTO (black), Au (blue), Cu deposited at -0.55 V vs RHE (green) and Cu deposited at -0.25 V vs RHE (red)

A clear nucleation behavior is found for Cu_2O@FTO electrodes (black line in **Fig 6**) where the current has a double slope inversion. This behavior was reported earlier [63] and interpreted as a 2D instantaneous nucleation mechanism (IN-2D) of Cu_2O on FTO, where nuclei are formed at the beginning of the electric pulse. The first layer is then the one controlling the shape and the morphology of the following ones. As evident, current initially decreases, then increases up to a maximum (about 75 s), then decreases towards a plateau than joins the other curves. This complex trend is related to the co-existence of different phenomena. The first peak is mainly related to the charge of the double layer followed by the adsorption of Cu(I) lactate species onto the clean substrate. While on Au and Cu the as formed Cu_2O is immediately oriented leading to a steady state current, on

FTO the initial grain formation is hindered, leading to an initial current decrease. Only after the current density minimum the formation of the first nucleus of Cu_2O occurs with a decrease in the recorded deposition current with growth of the Cu_2O layer.

To further analyze the differences between the Cu(0) electrodeposited at -0.25 and at -0.55 V, Pb UPD analysis, spectrophotometer measurements, LSV in dark and X-ray absorption spectroscopy (XAS) measurements were carried out.

In more detail, the active surface and crystallite orientation of the deposited layer was studied by Pb underpotential deposition (UPD)[73]. **Fig 7** reports the results obtained on Cu deposits formed at different potentials: -0.25 and -0.55 V (II and III potential, respectively, in **Fig 7**). Two other potentials have been added: 0.15 V (I Potential) and -0.85 V (IV Potential), the latter to evaluate the influence of strong hydrogen evolution during the Cu deposition.

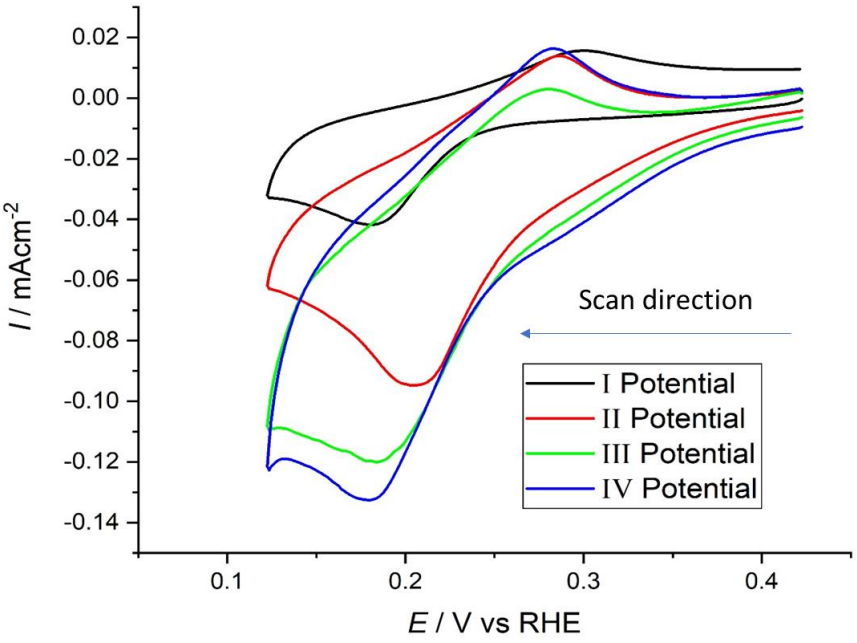

Fig 7 UPD measurements on Cu@FTO deposited at different potentials. I) -0.145 V vs RHE, II) -0.25 V vs RHE, III) -0.55 V vs RHE and IV) -0.85 V vs RHE. UPD bath: $Pb(OAc)_2$ 0.01 M, $NaClO_4$ 0.5 M and $HClO_4$ 0.001 M at pH 5.5. Scan rate 5 mVs^{-1}, counter electrode: Pt

The results for III and IV are rather similar, while I shows a much smaller charge (i.e. smaller surface area available). All the three samples present the same UPD potential, 0.185 V vs RHE. In the case of II, the peak potential is markedly different, possibly denoting a difference in terms of the preferentially exposed faces.

According to these results, potential II and III represent the best choice for underlayer characterization because they show high surface area (probably template by hydrogen bubbles) and opens the possibility of studying two different exposed crystal orientations. Indeed, from literature[57, 74] the UPD peak are expected to be at well-defined potentials according to the different exposed facets. In particular, the (111) facet likely cause the comparison of a single peak at 0.188 V, the (100) two peaks at 0.150 and at 0.178 V, while in case of the (110), the peaks are expected at 0.178 and 0.193 V. It was not possible to clearly identify the main exposed facet given the polycrystalline nature of the present material, but the presence of a single peak confirms the preferential orientation in the (111) facet, as already suggested by XRD.

Indeed, considering a total charge of 310 $\mu C \cdot cm^{-2}$ to deposit a monolayer of Pb[75], it is possible to estimate the Cu surface area:

$$Area = \frac{Q_{\mathrm{Pb}}}{Q_{\mathrm{S}}}$$

Where Q_{Pb} is the (background corrected) peak charge of Pb-UPD while Q_{S} is the specific charge for the UPD peak. The integrated charges are highly reproducible, and the average surface area results are 2.40 cm^2 and 1.85 cm^2 for samples deposited at -0.25 V and -0.55 V, respectively.

The color of underlayer/Cu_2O samples (see **Fig S1** in SI) depends on the potential applied for electrodeposition of Cu(0) layers. Therefore, spectroscopic measurements in UV-Vis-NIR range were performed to study the differences between samples.

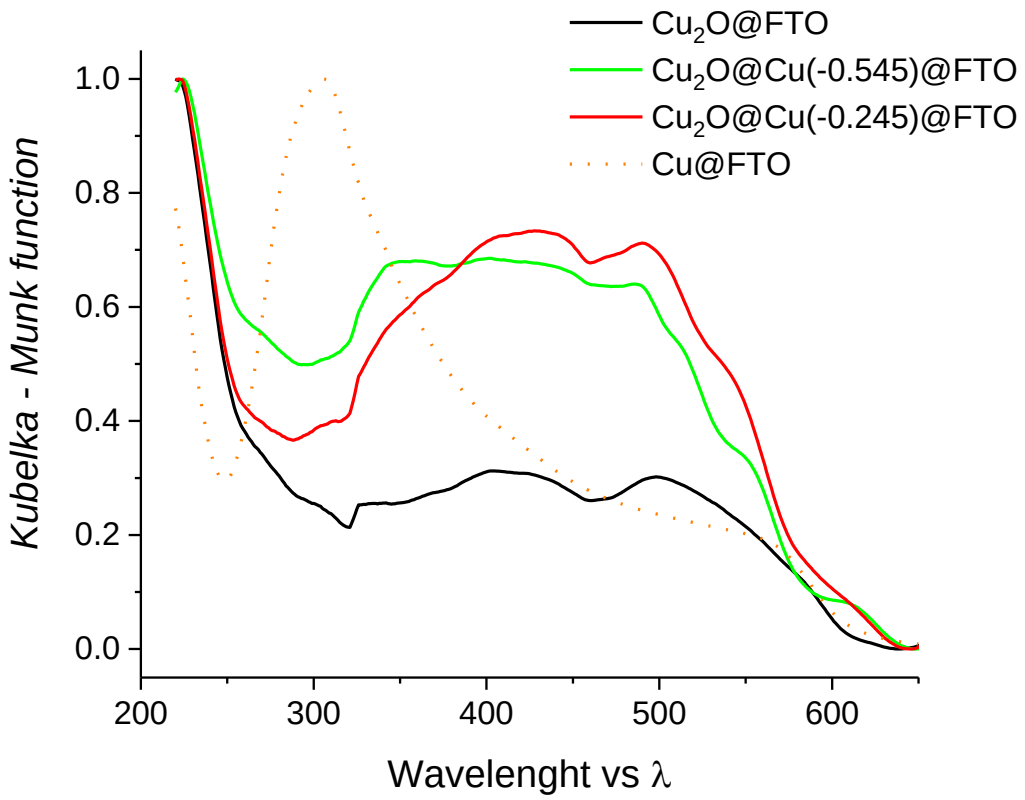

Fig 8 Absorption spectra of 3 different supported Cu_2O electrodes; Cu_2O@Cu(-0.25 V)@FTO (red), Cu_2O@Cu(-0.55 V)@FTO (green) and Cu_2O@FTO (black) recorded with integral sphere. The spectra of Cu(-0.55 V)@FTO)dashed, orange line) is also reported.

Diffuse reflectance spectra, converted by the Kubelka-Munk function, are presented in **Fig 8**. The spectra derive from the multilayered structure but clearly show an absorption peak between 400 and 500 nm that markedly grows in the presence of the metallic underlayer. This could likely be due to an absorption from the metallic layer under the semiconductor, as proved by the reflectance spectra of a Cu(-0.55 V)@FTO underlayer (dashed, orange curve), that absorbs in the considered range, but whose effect is not additive, being faded out by the Cu_2O overlayer.

According to the Tauc theory[76], for a direct semiconductors the band gap energy, E_{BG}, and the absorption coefficient, α, follow the relationship: $\alpha E \sim (E\text{-}E_{BG})^{1/2}$ where E is the photon energy. Since KM (Kubelka-Munk function) is proportional to α, the following relationship is fulfilled: $(KM \cdot E)^{1/2} \sim (E\text{-}E_{BG})$. Therefore, from the $(KM*E)^{1/2}$ vs E plots the band gap energy can be determined as shown

in **Fig 9**. The calculated band gap energies are 1.94 ± 0.01 eV, 1.92 ± 0.01 eV and 1.90 ± 0.01 eV for Cu_2O@FTO, Cu_2O@Cu(-0.25 V)@FTO and Cu_2O@Cu(-0.55 V)@FTO respectively. The use of a Cu underlayer just slightly affect the band gap energy: E_{BG} is larger in case of Cu_2O deposited directly onto FTO and decreases with decreasing potential of Cu underlayer deposition.

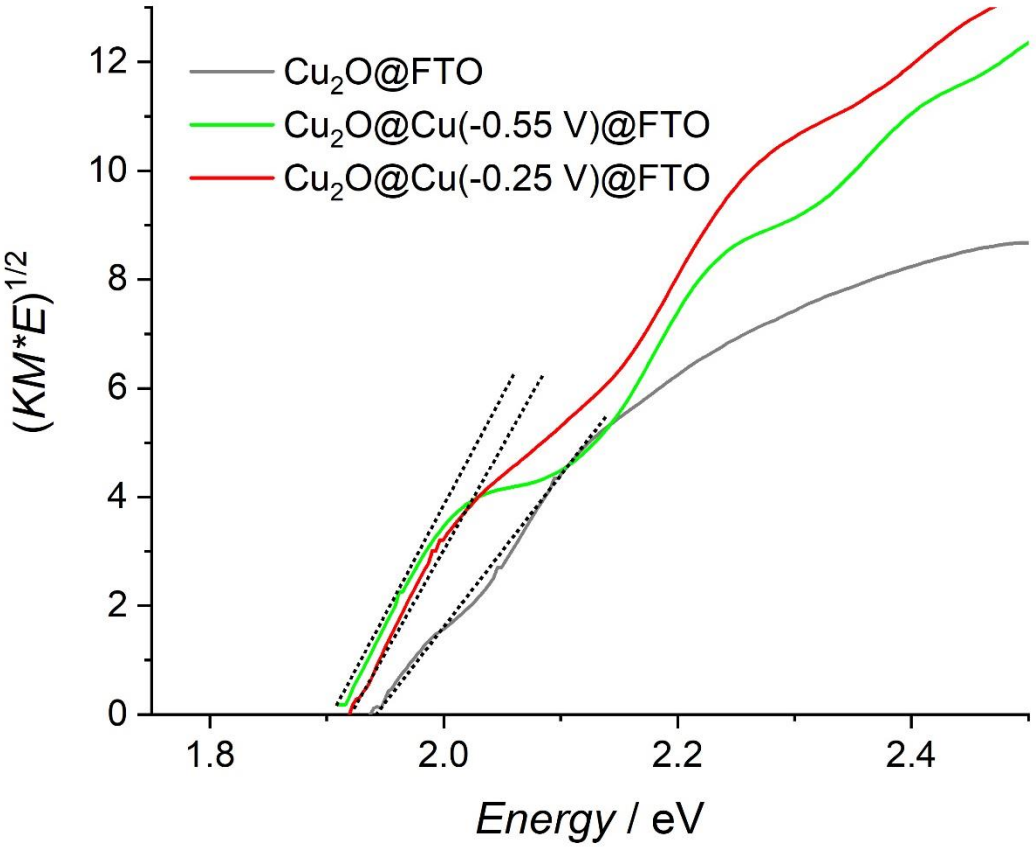

Fig 9 Tauc plots of Cu_2O@FTO (black), Cu_2O@Cu(-0.55 V)@FTO (green) and Cu_2O@Cu(-0.25 V)@FTO (red). Dotted lines are used to extrapolate the BG.

Differences in the Tauc plot intercepts can be resulting, in the present case, either from a change in the band gap or from the impact of a not fully transparent film (the underlayer) on the diffuse reflectance of Cu_2O. However, the observed differences are rather small and within experimental error of ± 0.01 eV. Moreover, the effect of these differences cannot explain the different behavior observed in the various samples.

Linear sweep voltammetries of Cu_2O@FTO, Cu_2O@Cu(-0.25V)@FTO and Cu_2O@Cu(-0.55 V)@FTO were performed in the dark at 10 $mV \cdot s^{-1}$ and are reported in **Fig 10**. The onset potential for the reduction to metallic Cu, likely followed by the HER, is clearly dependent on the presence of the underlayer and on its nature, the most stable semiconductor being the one deposited on Cu(-0.55 V), followed by the one deposited on Cu(-0.25 V) and finally by pure Cu_2O. Tuning the reduction potential represents a clear advantage for the dark stability of the semiconductor. This will allow to use the semiconductor at higher potential (and thus with higher current and available power) before the electrochemical reduction starts.

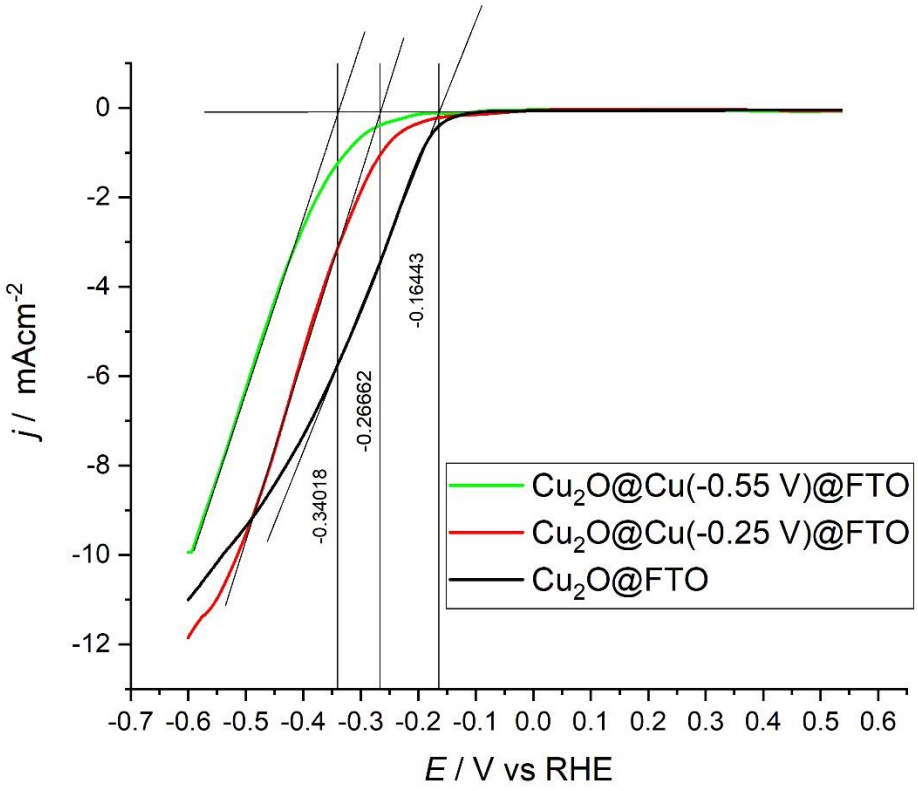

Fig 10 Electrochemical reduction in dark of Cu_2O@Cu(-0.55 V)@FTO (green), Cu_2O@Cu(-0.25 V)@FTO (red) , Cu_2O@ FTO (black). Linear Sweep Voltammetries performed in Na_2SO_4 0.5 M + NaOH 0.5 M (pH 11) at 10 mVs^{-1}

This marked difference is likely due to the presence of Cu that induces a shift in the reduction of Cu_2O or by an electronic effect of the buried Cu/Cu_2O junction. Indeed, the presence of metallic Cu could likely shift the following equilibrium:

$$2Cu^{+} \rightleftarrows Cu + Cu^{2+}$$ [5]

And change the formal potential of the reaction

$$Cu_2O + 2e^{-} + 2H^{+} \rightleftarrows 2Cu + H_2O$$ [6]

That is the one that causes the deactivation of Cu_2O photocathodes under photoelectrochemical conditions.

The difference induced by the two Cu underlayers can be explained by their different crystalline orientation, as evidenced by UPD experiments. It was indeed previously reported a higher stability of Cu_2O with (111) facet compared to other orientation due to different surface energy levels of conduction and valence band[71, 77]. Moreover, size and shape of Cu_2O particles could be slightly different because of co-morphological interaction between Cu_2O and Cu(0) leading to difference in stability and activity[78].

The role of the underlayer was evaluated from the structural point of view by XAS. Three Cu_2O electrodes were prepared on different substrates: FTO, Au@FTO (as a reference to the literature) and Cu@FTO. An EXAFS spectrum was recorded outside the solution for each kind of electrode and then compared with the Cu_2O standard pellet.

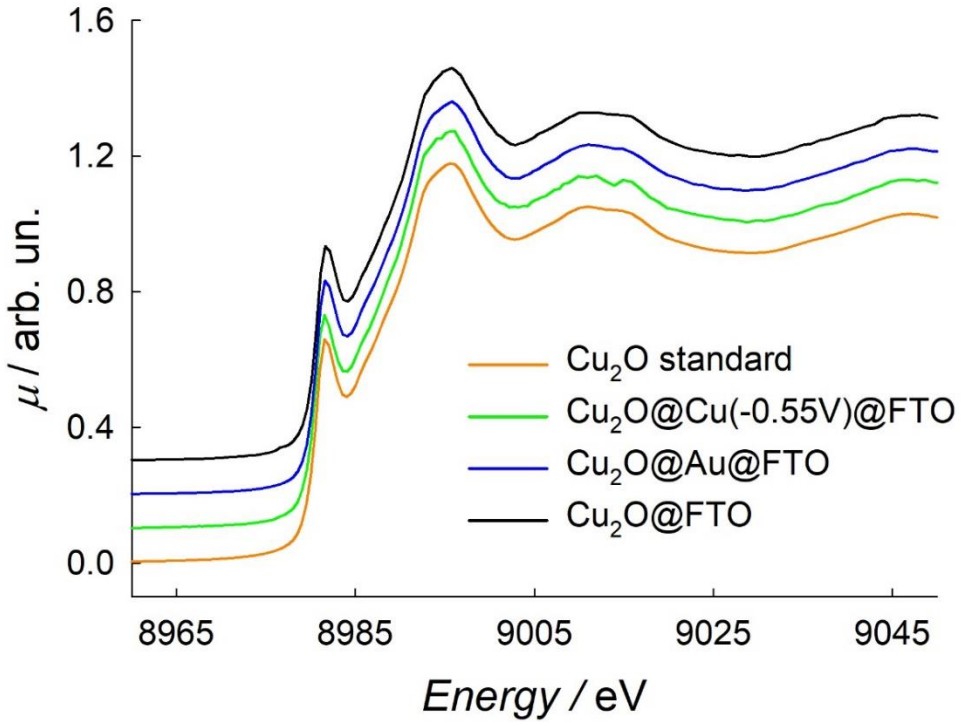

Fig 11 XAS spectra recorded at the Cu-K edge: Cu_2O standard (orange), Cu_2O@Au(PVD)@FTO (blue), Cu_2O@Cu(-0.55 V)@FTO (green), Cu_2O@FTO (black). The spectra are shifted on the y-axes for the sake of clarity

Comparison of the XANES spectra at the Cu-K edge with the spectrum of Cu_2O (**Fig 11**) shows that the oxidation state is Cu(I) for all samples. Therefore, any electronic effect of the buried Cu/Cu_2O junction, if present, is below the detection limit of this technique. To evaluate any possible differences in the chemical environment, the EXAFS spectra were fitted against a structural model derived from the crystal structure of Cu_2O. The results are shown in **Fig 12**, **13** and **14** and the fitting parameters are displayed in **Table**. **1**, **2** and **3 for** Cu_2O@Cu(-0.55 V)@FTO, Cu_2O@Au@FTO and Cu_2O@FTO respectively.

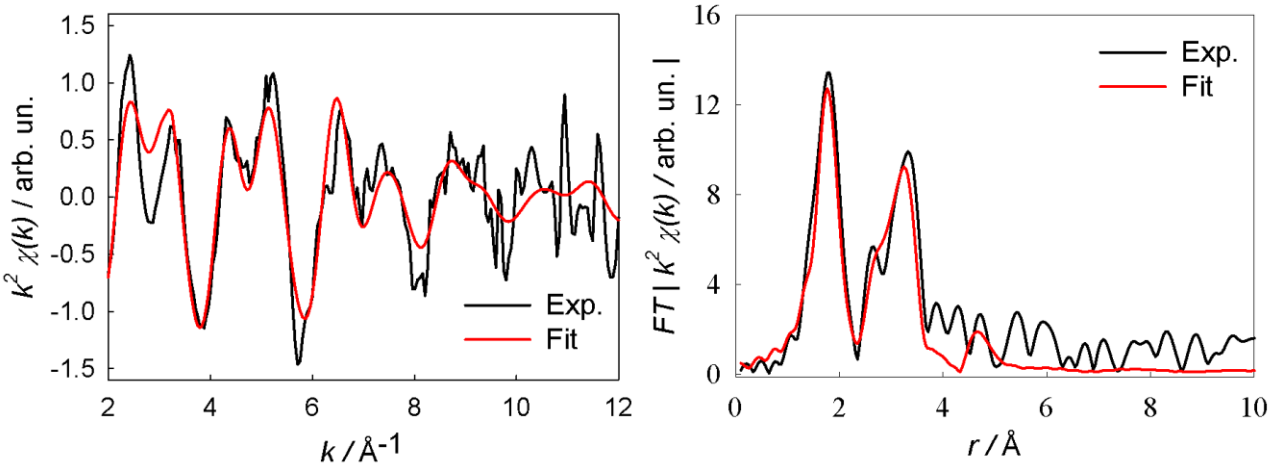

Fig 12 EXAFS spectra (on the left) and FT (on the right) for the Cu_2O@Cu(-0.55 V)@FTO electrode. The black line is the experimental data while the red one is the theoretical one after the fit

Table 1 Fitting parameters for the local surrounding of Cu in the Cu_2O@Cu(-0.55 V)@FTO electrode

Shell	N	Atom	r (Å)	σ^2 (Å^2)	r_0 (Å)*
1	2	O	1.90(2)	0.007(3)	1.849
2	6	Cu	2.94(2)	0.010(2)	3.019
3	6	Cu	3.10(2)	0.010(2)	3.019

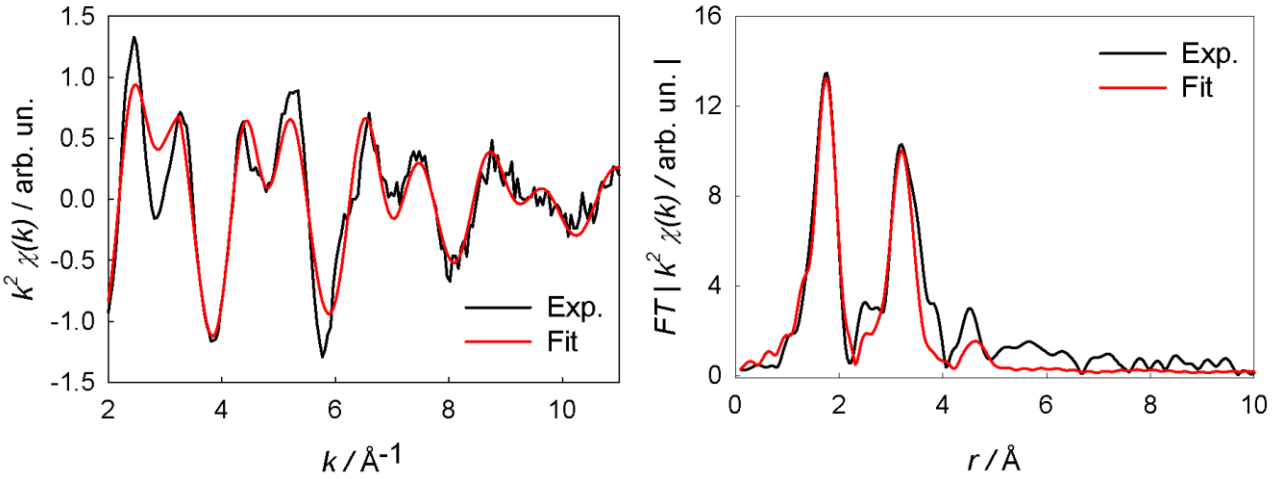

Fig 13 EXAFS spectra (on the left) and FT (on the right) for the Cu_2O@Au@FTO electrode. The black line is the experimental data while the red one is the theoretical one after the fit

Table 2 Fitting parameters for the local surrounding of Cu in the Cu_2O@Au@FTO electrode

Shell	N	Atom	r (Å)	σ^2 (Å^2)	r_0 (Å)*
1	2	O	1.89(2)	0.009(2)	1.849
2	6	Cu	2.89(3)	0.020(6)	3.019
3	6	Cu	3.04(2)	0.012(2)	3.019

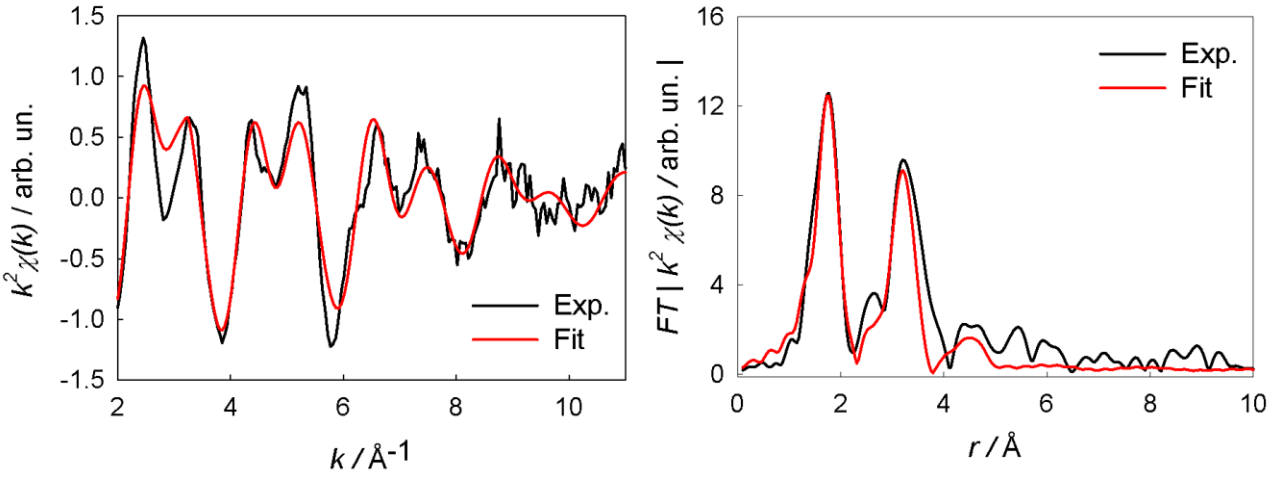

Fig 14 EXAFS spectra (on the left) and FT (on the right) for the Cu_2O@FTO electrode. The black line is the experimental data while the red one is the theoretical one after the fit.

Table 3 Fitting parameters for the local surrounding of Cu in the Cu_2O@FTO electrode

Shell	N	Atom	r (Å)	σ^2 (Å^2)	r_0 (Å)*
1	2	O	1.89(2)	0.010(2)	1.849
2	6	Cu	2.90(4)	0.021(8)	3.019
3	6	Cu	3.04(2)	0.014(3)	3.019

EXAFS spectra show no differences, within the experimental error, in the structural parameters of the different samples, thus leading to the conclusion that the presence of different underlayers does not change the local chemical surrounding of Cu_2O. However, when compared to the parameters

derived from the crystal structure of Cu_2O (r_0 in **Table 1**, **2** and **3**), significant distortions can be observed for all the samples. The second coordination shell of Cu in Cu_2O is made up by 12 Cu atoms divided in two subsets of 6 atoms each. A marked contraction in the coordination distance is observed for the first subset, while a slight expansion is observed for the second set. If the crystal structure is projected along the (111) direction, then the first subset makes a hexagon of Cu atoms surrounding the central Cu, while the second subset furtherly divides in two subsets of three Cu atoms, one subset being above and the other below the plane of the hexagon. Thus, both the contraction and the expansion of the coordination distances of the two second neighbor shells can be attribute to the film nature of the samples.

3.4 Photoactivity studies

The performances of Cu_2O without and with different underlayers, Cu(-0.25 V), Cu(-0.55 V) and Au, were tested under solar simulated light. Results are summarized in **Fig 15**.

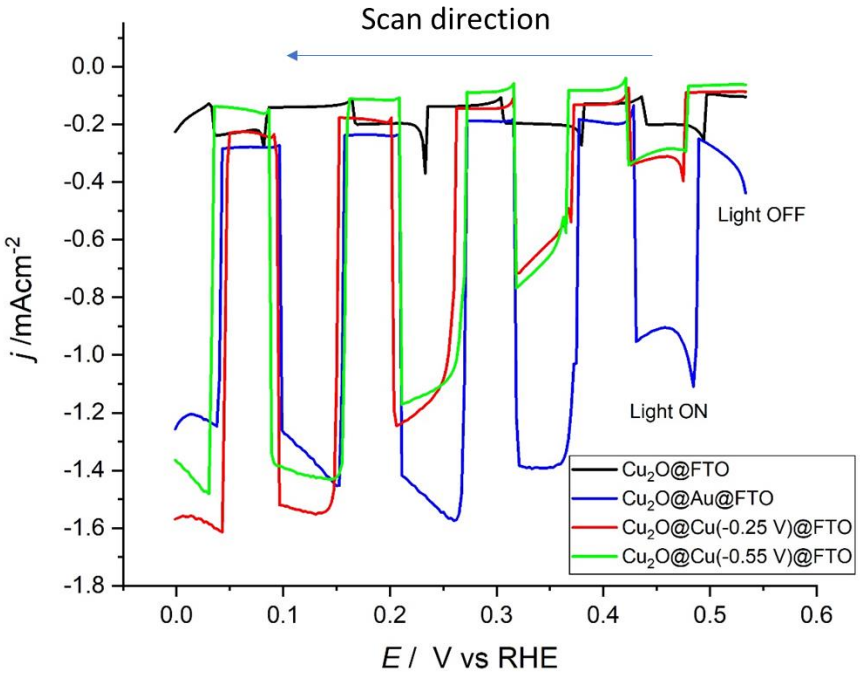

Fig 15 Linear Sweep Voltammetries at 10 mVs^{-1} performed in 0.5 M Na_2SO_4 +0.5 M NaOH (pH 11) on differently supported electrodes. Cu_2O@Au@FTO (blue), Cu_2O@Cu(-0.25 V)@FTO (red), Cu_2O@FTO (black) and Cu_2O@Cu(-

0.55 V)@FTO (green). Measurements under pulsed solar simulator light (1.5 AM) in N_2-purged solution. Counter electrode: Pt

All curves were recorded on three samples and the results were reproducible. In the complete absence of underlayers (black curve) photocurrents are one order of magnitude lower than in the presence of a metallic support. The presence of a metallic underlayer strongly affects the amount of hydrogen produced by the semiconductor. In particular, Au allows the generation of high cathodic photocurrents at lower potentials (red curve) while Cu presents higher photocurrents at more negative potential, (green and red curves below 0.2 V). The analysis of Cu(0) electrochemical deposition revealed two different cathodic peaks, with some differences in the physicochemical properties of the deposited Cu. In spite of this, the two methods to deposit Cu seem to not substantially affect the Cu_2O photo-behavior, leading to similar photocurrents, meaning that the final performances are mostly affected by the chemical nature of the metallic underlayer. This is not related to structural difference of the Cu_2O deposit, rather to an improved hole conduction (that prevents electron-hole recombination) and possibly to a partial light reflection from the underlayer.

Further effects induced by the metallic underlayer could be due by lattice strain induced by the lattice mismatch between semiconductor and metallic underlayer[80] and by possible doping from or to the metallic underlayer with an increase/decrease of semiconductor vacancies; or even to an increase in the number of light-generated electrons coming from the material.

These possibilities are under study but require an *ad-hoc* sample preparation, including the study of mono/multiatomic semiconductor layers on the substrate (the strain effect can fade in a "massive" deposit) and/or by heat treatments (doping from the underlayer).

However, the analysis of dark current reveal further outcomes. As earlier suggested by dark LSV (**Fig 10**), sample Cu_2O@Cu(-0.55 V)@FTO shows a wider stability window, testified by current densities in the dark (due to Cu_2O electroreduction) that are lower than the other samples. This effect will be the bases for future work, pointing at composite electrode with improved stability.

Indeed, Cu_2O@Cu@FTO should also present a higher stability in water solution under illumination according to Huang et al. because photoelectrons can be drained to the Cu core minimizing the probability of Cu_2O photodegradation[79].

3.5 Influence of Underlayer Loading

The effects of the Cu underlayer loading and morphology were investigated and demonstrated to be easily tunable, in terms of thickness and homogeneity, by controlling the time, and thus the quantity of charge, of the electrodeposition. A similar approach was carried out for the Cu_2O and the results are presents in the supporting information (**Fig S2**). In fact, H_2 evolution plays an evident role only at -0.55 V. This was further confirmed by calibration experiments, where high loaded samples (at -0.25 and -0.55 V) were weighted using an analytical balance.

Table 4 shows the total amount of passed charge, *Q*, and the thickness, *l*, of Cu layer, considering a 100% current efficiency for the deposition process.

Table 4 Summary of the electrodes tested with different underlayer loadings reported as charge passed through the electrode

***Q* / C**	***l* / μm**
2.5	0.92
1	0.35
0.47	0.17
0.25	9.19×10^{-2}
0.13	4.78×10^{-2}

This value is calculated using the following equation:

$$l = \frac{Q*M}{n*96485} * \frac{1}{d} * \frac{1}{A} \quad [7]$$

Where l is the thickness, Q the integrated quantity of charge, M the molar mass, n the number of electrons, F the faraday constant, d the Cu density and A electrode geometric area, 1 cm^2.

Fig 16 reports the photocurrent densities recorded on Cu_2O@Cu(-0.55 V)@FTO electrodes having different loadings (thicknesses) of Cu(0), from 0.13 C to up to 2.5 C (20 times higher). The photocurrent increases with the increase of deposited Cu(0) amount, reaching a plateau at 0.5 C. This is likely due to the metallic layer capability of effectively transfer photogenerated holes until the homogeneity of the deposit reaches its best. Higher loads do not lead to a photocurrent increase. The charge of 0.47 C is considered as the optimal value to avoid a bulky deposition of metallic Cu, that can drastically reduce the composite electrode transparency, still guaranteeing the maximum performances. Similar experiments were performed to study how tuning the Cu_2O amount will affect the final photocurrent (see **Supporting Information**).

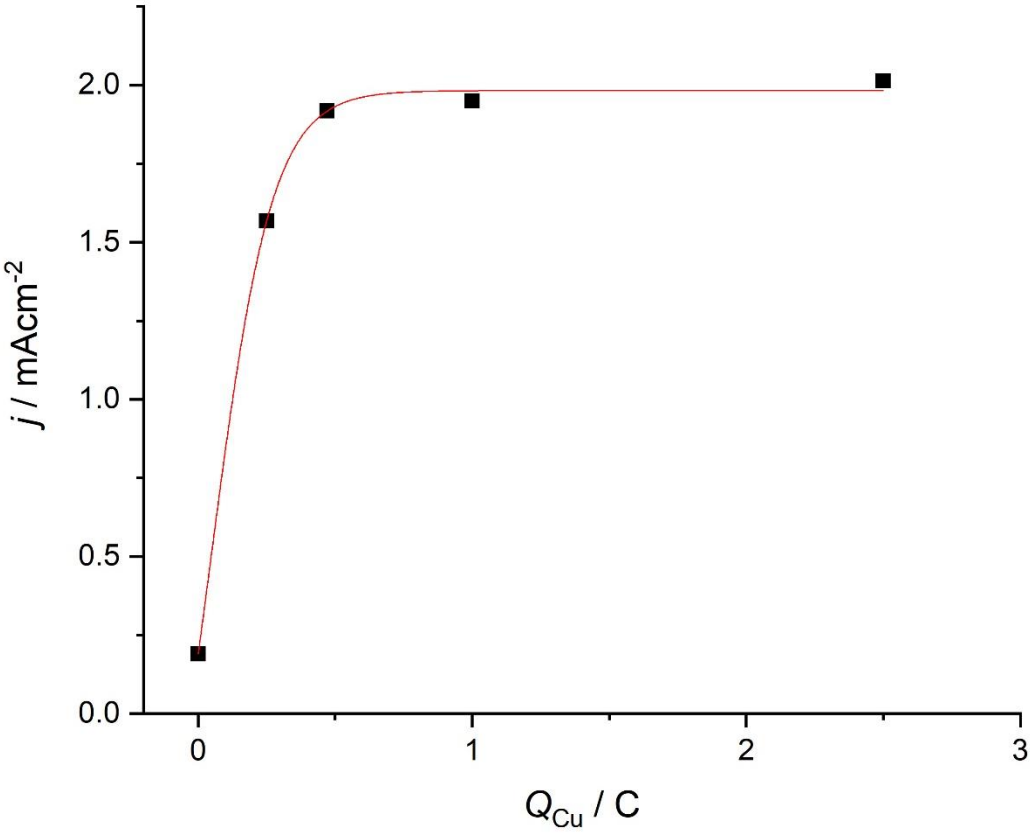

Fig 16 Photocurrent densities recorded on Cu_2O@Cu(-0.55 V)@FTO with different amount of Cu. Photocurrent densities are reported in absolute value for sake of clarity

4. Conclusion

In conclusion, this paper evidences the great importance of the presence of a metallic underlayer in Cu_2O PEC-WS photocathode performance, attested by the increase of almost one order of magnitude in photocurrent values by a correct tuning of the deposition of a metallic substrate.

The present work demonstrates that metallic Cu is a promising candidate as Cu_2O underlayer, able to increase the produced photocurrent with respect to the absence of an underlayer. It is worthwhile to underline that Cu is indeed a low-cost, non-toxic material that can be easily electrodeposited from the same Cu_2O deposition bath, leading to an easy scale up of the entire setup. The obtained photocurrents

are comparable with those obtained with Au underlayers, but the reduced cost could be attractive to develop this technology more in order to really use PEC-WS systems as energy storage solution.

Interestingly, the sample based on the underlayer deposited at -0.55 V shows improvements in terms of the photoelectrode stability.

Finally, increasing the thickness of the metallic underlayer leads to an improvement in the photoelectrode performance until a plateau is reached.

5. Acknowledgment

We thankfully acknowledge beamline BM08 “LISA” at the European Synchrotron Radiation Facility for provision of beamtime (experiment 08-01-1004) and Francesco D’Acapito for the kind support during the experiment. Università degli Studi di Milano by the “Piano di Sostegno alla Ricerca” is gratefully acknowledged. The Authors are thankful to Dr. Adriano Gomes for his help in ex-situ characterizations with SEM and XRD.

Bibliography

1. Rodriguez CA, Modestino MA, Psaltis D, Moser C (2014) Design and cost considerations for practical solar-hydrogen generators. Energy Environ Sci 7:3828–3835.

2. Ager JW, Shaner MR, Walczak KA, et al (2015) Experimental demonstrations of spontaneous, solar-driven photoelectrochemical water splitting. Energy Environ Sci 8:2811–2824.

3. Pinaud BA, Benck JD, Seitz LC, et al (2013) Technical and economic feasibility of centralized facilities for solar hydrogen production via photocatalysis and photoelectrochemistry. Energy Environ Sci 6:1983–2002.

4. Jiang C, Moniz SJA, Wang A, et al (2017) Photoelectrochemical devices for solar water splitting-materials and challenges. Chem Soc Rev 46:4645–4660.

5. Jiménez Reinosa J, Leret P, Álvarez-Docio CM, et al (2016) Enhancement of UV absorption behavior in ZnO-TiO_2 composites. Bol la Soc Esp Ceram y Vidr 55:55–62.

6. Tang SJ, Moniz SJA, Shevlin SA, et al (2015) Visible-light driven heterojunction photocatalysts for water splitting – a critical review. Energy Environ Sci 8:731–759.

7. Chen S, Wang L-W (2012) Thermodynamic Oxidation and Reduction Potentials of Photocatalytic Semiconductors in Aqueous Solution. Chem Mater 24:3659–3666.

8. Bagal I V., Chodankar NR, Hassan MA, et al (2019) Cu_2O as an emerging photocathode for solar water splitting - A status review. Int J Hydrogen Energy 44: 21351–21378

9. Lloyd MA, Siah SC, Brandt RE, et al (2016) Intrinsic defect engineering of cuprous oxide to enhance electrical transport properties for photovoltaic applications. Conf Rec IEEE Photovolt Spec Conf :3443–3445.

10. Jiang Y, Yuan H, Chen H (2014) Enhanced visible light photocatalytic activity of Cu_2O via cationic-anionic passivated codoping. Phys Chem Chem Phys 17:630–7.

11. Musa AO, Akomolafe T, Carter MJ (1998) Production of cuprous oxide, a solar cell material, by thermal oxidation and a study of its physical and electrical properties. Sol Energ Mat Sol Cell 51:305–316

12. Hsu YK, Yu CH, Chen YC, Lin YG (2013) Fabrication of coral-like Cu_2O nanoelectrode for solar hydrogen generation. J Power Sources 242:541–547.

13. Lim Y-F, Chua CS, Lee CJJ, Chi D (2014) Sol–gel deposited Cu_2O and CuO thin films for photocatalytic water splitting. Phys Chem Chem Phys 16:25928–25934.

14. Wei M, Huo J (2010) Preparation of Cu_2O nanorods by a simple solvothermal method. Mater Chem Phys 121:291–294.

15. Wei M, Lun N, Ma X, Wen S (2007) A simple solvothermal reduction route to copper and cuprous

oxide. Mater Lett 61:2147–2150.

16. Barreca D, Comini E, Gasparotto A, et al (2009) Chemical vapor deposition of copper oxide films and entangled quasi-1D nanoarchitectures as innovative gas sensors. Sensors Actuators, B Chem 141:270–275.

17. Wang S, Zhang X, Pan L, et al (2015) Controllable sonochemical synthesis of $Cu_2O/Cu_2(OH)_3NO_3$ composites toward synergy of adsorption and photocatalysis. Appl Catal B Environ 164:234–240

18. Ma D, Liu H, Yang H, et al (2009) High pressure hydrothermal synthesis of cuprous oxide microstructures of novel morphologies. Mater Chem Phys 116:458–463.

19. Valodkar M, Pal A, Thakore S (2011) Synthesis and characterization of cuprous oxide dendrites: New simplified green hydrothermal route. J Alloys Compd 509:523–528.

20. Togashi T, Hitaka H, Ohara S, et al (2010) Controlled reduction of Cu^{2+} to Cu^{+} with an N,O-type chelate under hydrothermal conditions to produce Cu_2O nanoparticles. Mater Lett 64:1049–1051.

21. Neskovska R, Ristova M, Velevska J, Ristov M (2007) Electrochromism of the electroless deposited cuprous oxide films. Thin Solid Films 515:4717–4721.

22. Itoh T, Maki K (2007) Growth process of CuO(111) and Cu_2O(001) thin films on MgO(001) substrate under metal-mode condition by reactive dc-magnetron sputtering. Vacuum 81:1068–1076.

23. Daltin AL, Bohr F, Chopart JP (2009) Kinetics of Cu_2O electrocrystallization under magnetic fields. Electrochim Acta 54:5813–5817.

24. Golden TD, Shumsky MG, Zhou Y, et al (1996) Electrochemical Deposition of Copper(I) Oxide Films. Chem Mater 8:2499–2504.

25. Paracchino A, Laporte V, Sivula K, et al (2011) Highly active oxide photocathode for photoelectrochemical water reduction. Nat Mater 10:456–461.

26. Paracchino A, Brauer JC, Moser J-E, et al (2012) Synthesis and characterization of high-photoactivity electrodeposited Cu_2O solar absorber by photoelectrochemistry and ultrafast spectroscopy. J Phys Chem C 116:7341–7350

27. Lin C, Lai Y, Mersch D, Reisner E (2012) $Cu_2O|NiO_x$ nanocomposite as an inexpensive photocathode in photoelectrochemical water splitting. Chem Sci 3:3482–3487.

28. Elfadill NG, Hashim MR, Chahrour KM, Mohammed SA (2016) Preparation of p-type Na-doped Cu_2O by electrodeposition for a p-n homojunction thin film solar cell. Semicond Sci Technol 31:065001.

29. Mahalingam T, Chitra JS., Rajendran S, et al (2000) Galvanostatic deposition and characterization of cuprous oxide thin films. J Cryst Growth 216:304–310.

30. Daltin AL, Addad A, Chopart JP (2005) Potentiostatic deposition and characterization of cuprous oxide films and nanowires. J Cryst Growth 282:414–420.

31. Mahalingam T, Chitra JSP, Chu JP, Sebastian PJ (2004) Preparation and microstructural studies of electrodeposited Cu_2O thin films. Mater Lett 58:1802–1807.

32. Wu G, Zhai W, Sun F, et al (2012) Morphology-controlled electrodeposition of Cu_2O microcrystalline particle films for application in photocatalysis under sunlight. Mater Res Bull 47:4026–4030.

33. Wang L, Tao M (2007) Fabrication and Characterization of p-n Homojunctions in Cuprous Oxide by Electrochemical Deposition. Electrochem Solid-State Lett 10:H248–H250.

34. Yoon S, Kim M, Kim I-S, et al (2014) Manipulation of cuprous oxide surfaces for improving their photocatalytic activity. J Mater Chem A 2:11621.

35. Wang LC, de Tacconi NR, Chenthamarakshan CR, et al (2007) Electrodeposited copper oxide films: Effect of bath pH on grain orientation and orientation-dependent interfacial behavior. Thin Solid Films 515:3090–3095.

36. Scanlon DO, Watson GW (2010) Undoped n-type Cu_2O: Fact or fiction?. J Phys Chem Lett 1:2582–2585

37. Nian JN, Hu CC, Teng H (2008) Electrodeposited p-type Cu_2O for H_2 evolution from photoelectrolysis of water under visible light illumination. Int J Hydrogen Energy 33:2897–2903.

38. Elmezayyen A, Guan S, Reicha FM, et al (2015) Effect of conductive substrate (working electrode) on the morphology of electrodeposited Cu_2O. J Phys D Appl Phys 48:175502

39. Wang G, van den Berg R, de Mello Donega C, et al (2016) Silica-supported Cu_2O nanoparticles with tunable size for sustainable hydrogen generation. Appl Catal B Environ 192:199–207

40. Paracchino A, Brauer JC, Moser J-E, et al (2012) Synthesis and Characterization of High-Photoactivity Electrodeposited Cu_2O Solar Absorber by Photoelectrochemistry and Ultrafast Spectroscopy. J Phys Chem C 116:7341-7350

41. Fernando CAN, De Silva l. AA, Takahashi K (2001) Junction effects of p-Cu_2O photocathode with layers of hole transfer sites (Au) and electron transfer sites (NiO) at the electrolyte interface. Semicond Sci Technol 16:433–439

42. Zhang S, Jiang R, Guo Y, et al (2016) Plasmon Modes Induced by Anisotropic Gap Opening in Au@Cu_2O Nanorods. Small 12:4264–4276.

43. Mahmoud MA, Qian W, El-Sayed MA (2011) Following charge separation on the nanoscale in Cu_2O-Au nanoframe hollow nanoparticles. Nano Lett 11:3285–3289.

44. Lan T, Mundt C, Tran M, Padalkar S (2017) Effect of gold underlayer on copper(I) oxide photocathode performance. J Mater Res 32:1656–1664.

45. Lan T, Padalkar S (2017) Exploring the Influence of Au Underlayer Thickness on Photocathode Performance. ECS Trans 80:1049–1055.

46. Parliament E, Agency EC (2014) Commission Regulation (EU) No 301/2014, amending Annex XVII to Regulation (EC) No 1907/2006 of the European Parliament and of the Council on the Registration, Evaluation, Authorisation and Restriction of Chemicals (REACH) as regards chromium VI compounds

47. Jin Z, Hu Z, Yu JC, Wang J (2016) Room temperature synthesis of a highly active Cu/Cu_2O photocathode for photoelectrochemical water splitting. J Mater Chem A 4:13736–13741.

48. Tang C, Ning X, Li J, et al (2019) Modulating conductivity type of cuprous oxide (Cu_2O) films on

copper foil in aqueous solution by comproportionation. J Mater Sci Technol 35:1570–1577.

49. Jung K, Lim T, Bae H, et al (2019) Cu_2O Photocathode with Faster Charge Transfer by Fully Reacted Cu Seed Layer to Enhance Performance of Hydrogen Evolution in Solar Water Splitting Applications. ChemCatChem 11, 4377-4382.

50. Matula RA (1979) Electrical resistivity of copper , gold palladium , and silver. J Phys Chem Ref. Data 8:1147–1298.

51. Achilli E, Vertova A, Visibile A, et al (2017) Structure and Stability of a Copper(II) Lactate Complex in Alkaline Solution: A Case Study by Energy-Dispersive X-ray Absorption Spectroscopy. Inorg Chem 56:6982–6989.

52. Liu G, Wang L, Xue D (2010) Synthesis of Cu_2O crystals by galvanic deposition technique. Mater Lett 64:2475–2478.

53. Tang Y, Chen Z, Jia Z, et al (2005) Electrodeposition and characterization of nanocrystalline cuprous oxide thin films on TiO2 films. Mater Lett 59:434–438

54. Septina W, Ikeda S, Khan MA, et al (2011) Potentiostatic electrodeposition of cuprous oxide thin films for photovoltaic applications. Electrochim Acta 56:4882–4888.

55. Wijesundera RP, Hidaka M, Koga K, et al (2006) Growth and characterisation of potentiostatically electrodeposited Cu_2O and Cu thin films. Thin Solid Films 500:241–246.

56. Mathew X, Mathews NR, Sebastian PJ (2001) Temperature dependence of the optical transitions in electrodeposited Cu_2O thin films. Sol Energy Mater Sol Cells 70:277–286.

57. Vilche JR, Juttner K (1987) Anion effects on the underpotential deposition of lead on Cu(111). Electrochim Acta 32:1567–1572

58. Brisard GM, Zenati E, Gasteiger HA, et al (1996) Underpotential Deposition of Lead on Copper (l11): A Study Using a Single-Crystal Rotating Ring Disk Electrode and ex Situ Low-Energy Electron Diffraction and Auger Electron Spectroscopy. Langmuir 11:2221-2230

59. Ravel B, Newville M (2005) ATHENA , ARTEMIS, HEPHAESTUS : data analysis for X-ray

absorption spectroscopy using IFEFFIT. J Synchrotron Radiat 12:537–541.

60. Newville M (2001) IFEFFIT: interactive XAFS analysis and FEFF fitting. J Synchrotron Radiat 8:322–324.

61. Yang Y, Li Y, Pritzker M (2016) Control of Cu_2O Film Morphology Using Potentiostatic Pulsed Electrodeposition. Electrochim Acta 213:225–235

62. Zhang Z, Wang P (2012) Highly stable copper oxide composite as an effective photocathode for water splitting via a facile electrochemical synthesis strategy. J Mater Chem 22:2456–2464.

63. Bijani S, Schrebler R, Dalchiele EA, et al (2011) Study of the nucleation and growth mechanisms in the electrodeposition of micro- and nanostructured Cu_2O thin films. J Phys Chem C 115:21373–21382

64. Heng B, Xiao T, Hu X, et al (2011) Catalytic activity of Cu_2O micro-particles with different morphologies in the thermal decomposition of ammonium perchlorate. Thermochim Acta 524:135–139.

65. Huang L, Peng F, Yu H, Wang H (2009) Preparation of cuprous oxides with different sizes and their behaviors of adsorption, visible-light driven photocatalysis and photocorrosion. Solid State Sci 11:129–138

66. Kakuta S, Abe T (2009) Photocatalytic activity of Cu_2O nanoparticles prepared through novel synthesis method of precursor reduction in the presence of thiosulfate. Solid State Sci 11:1465–1469

67. Long J, Dong J, Wang X, et al (2009) Photochemical synthesis of submicron- and nano-scale Cu_2O particles. J Colloid Interface Sci 333:791–799.

68. Zhang X, Song J, Jiao J, Mei X (2010) Preparation and photocatalytic activity of cuprous oxides. Solid State Sci 12:1215–1219

69. Singh DP, Singh JAI, Mishra PR, et al (2008) Synthesis , characterization and application of semiconducting oxide (Cu_2O and ZnO) nanostructures. Bull Mater Sci 31:319–325

70. Zhou Y, Switzer JA (1998) Electrochemical deposition and microstructure of copper (I) oxide films.

Scr Mater 38:1731–1738

71. Ma QB, Hofmann JP, Litke A, Hensen EJM (2015) Cu_2O photoelectrodes for solar water splitting: Tuning photoelectrochemical performance by controlled faceting. Sol Energy Mater Sol Cells 141:178–186.

72. Heltemes EC (1966) Far-infrared properties of cuprous oxide. Phys Rev 141:803–805.

73. Siegenthaler H, Juttner K (1984) Voltammetric investigation of lead adsorption on Cu(111) single crystal substrates. J Electroanal Chem 163:327–343

74. Bewick A, Jovicevic J, Thomas B (1984) Phase formation in the underpotential deposition of metals. Faraday Symp Chem Soc 12:24–35

75. Bewick A, Jovićević J, Thomas B (1977) Phase formation in the underpotential deposition of metals. Faraday Symp Chem Soc 12:24–35.

76. Tauc J (1968) Optical properties and electronic structure of amorphous Ge and Si. Mater Res Bull 3:37–46.

77. Zheng Z, Huang B, Wang Z, et al (2009) Crystal faces of Cu_2O and their stabilities in photocatalytic reactions. J Phys Chem C 113:14448–14453.

78. Kwon Y, Soon A, Han H, Lee H (2015) Shape effects of cuprous oxide particles on stability in water and photocatalytic water splitting. J Mater Chem A 3:156–162.

79. Huang C-L, Weng W-L, Huang Y-S, Liao C-N (2019) Enhanced photolysis stability of Cu_2O grown on Cu nanowires with nanoscale twin boundaries . Nanoscale 11:13709-13713

80. Visibile A, Wang RB, Vertova A, et al (2019) Influence of Strain on the Band Gap of Cu_2O. Chem Mater. Chem Mater 31:4787-4792